Enhancing Potassium-Ion Storage through Nanostructure Engineering and Ion-Doped: A Case Study of Cu^{2+}-Doped $Co_{0.85}Se$ with Yolk-Shell Structure

Daming Chen[1], Yang Ming[1], Wei Cai[1], Zhen Wang[2], Benjamin Tawiah[1], Shuo Shi[1], Xin Hu[1], Rujun Yu[1], Chi-sun Poon[3], Bin Fei[1,*]

1. Materials Synthesis and Processing Lab, School of Fashion and Textiles, The Hong Kong Polytechnic University, Kowloon, Hong Kong SAR 999077, P. R. China

2. College of Chemistry and Molecular Engineering, Qingdao University of Science and Technology, Qingdao, 266042, P. R. China

3. Department of Civil and Environmental Engineering, The Hong Kong Polytechnic University, Kowloon, Hong Kong SAR 999077, P. R. China

* Corresponding author, E-mail: bin.fei@polyu.edu.hk

Abstract

Fabricating transition metal selenide (TMSe) anode materials with rapid K^+ diffusion and high-rate performance is crucial for the advancement of potassium-ion batteries (PIBs), yet it remains a challenge. In this study, we developed a Cu^{2+}-doped $Co_{0.85}Se$@N-doped carbon anode with an optimal concentration of Cu^{2+}-doped and yolk-shell structure (denoted as Cu-$Co_{0.85}Se$@NC-2) to enhance the reaction kinetics and cycling life. The Cu^{2+}-doped modulates the electronic structure of the $Co_{0.85}Se$ interface, improves the diffusion and adsorption of K^+, and further promotes the charge transport efficiency, as demonstrated by theoretical calculations and experimental results. In addition, we identified an optimal Cu^{2+}-doped content that is conducive to achieving the best structure and electrochemical performance. Moreover, the N-doped carbon shell effectively enhances the conductivity of the electrode and alleviates the volume change of $Co_{0.85}Se$ yolk during cycling. Benefiting from the above advantages, the obtained Cu-$Co_{0.85}Se$@NC-2 anode exhibits excellent rate performance (208.1 mA h g^{-1} at 10 A g^{-1}) and cycling stability (239.7 mA h g^{-1} at 2 A g^{-1} after 500 cycles, the capacity retention rate is up to 80.4%). This work integrates nanostructure engineering and ion-doped to provide a straightforward and effective strategy for designing advanced high-rate TMSe anodes for next-generation PIBs.

Keywords: Cu^{2+}-doped, electronic structure, reaction kinetics, yolk-shell structure, potassium-ion batteries

1. Introduction

Lithium-ion batteries (LIBs) have achieved widespread adoption in portable electronics and electric vehicles over recent decades, attributed to their superior energy density and longevity.[1-3] Nonetheless, the sustainable development of LIBs in large-scale energy storage applications is severely limited by lithium's scarcity, uneven geographical distribution, and high cost. Consequently, it has become an urgent need to develop low-cost and resource-rich metal resources (such as Na and K) to replace Li.[4, 5] Compared with the reserves of Li (20 ppm), the reserves of K in the earth's crust (17000 ppm) seem endless.[6, 7] Meanwhile, the redox potential of K (-2.94 V for K^+/K) is lower than that of Na (-2.71 V for Na^+/Na), so that potassium ion batteries (PIBs) can work at higher voltages, making it easier to obtain higher energy density.[8] Therefore, PIBs have garnered significant interest as an economical and high-capacity energy storage solution in recent years.[9, 10] However, the substantial ionic radius of K^+ (1.38 Å) leads to considerable electrode volume expansion and sluggish kinetics, adversely affecting stability and rate performance.[11] Therefore, the primary challenge facing the development of PIBs lies in the innovation of new anode materials designed to surmount these specific issues.

Transition metal chalcogenides (TMCs) have relatively high theoretical specific capacity and relatively small charge-discharge volume variation, which are considered to be one of the most promising anode electrode materials for PIBs.[12-14] Relative to transition metal sulfides, the weaker TM-Se bond of transition metal selenide (TMSe) is easily broken by K^+ in the conversion reaction, resulting in better reaction kinetics.[15, 16] Among the many TMSe, $Co_{0.85}Se$ is considered an attractive anode material for PIBs, owing to its superior energy storage performance.[17-19] Nevertheless, akin to other TMCs, challenges persist with $Co_{0.85}Se$, including unfavorable reaction kinetics, rapid capacity fade, and significant polarization issues stemming from low electronic conductivity and substantial volumetric changes during

electrochemical reactions.[10, 19, 20] Thus, there is still much room for improvement in the optimization of $Co_{0.85}Se$.

Optimization strategies, such as nanostructure engineering and carbon nanophase confinement, effectively alleviate the volume expansion and improve the electrochemical performance. Notably, materials derived from metal-organic frameworks can encapsulate active materials within carbon layers, forming yolk-shell structures. These structures furnish appropriate void spaces to accommodate the volumetric expansion of TMSe, thereby improving the ion/electron transfer kinetics of the composite material to a certain degree.[21-23] For example, Feng et al. reported a yolk-shell Zn-Co-Se@NDC nanostructure as an anode material that effectively relieved volume expansion and improved the reaction kinetics.[24] At the same time, our previous work utilized ZIF-8@ZIF-67 to in-situ synthesize yolk-shell structures at different selenization temperatures, effectively improving the electrochemical performance.[25] However, TMSe usually exists in the carbon nanophase in the form of a nanoscale structure, and the conductivity and kinetics are still insufficient.

To overcome the above problems, researchers have devised several strategies, including multiphase combination, ion-doped, and working voltage regulation.[26] Ion-doped, in particular, offers dual benefits: it not only adjusts the charge distribution within TMSe, enhancing reaction kinetics but also fine-tunes the van der Waals forces and the TM-Se band gap, facilitating a stable K^+ intercalation process.[27, 28] However, it has been observed that excessive ion-doped may compromise the structural integrity, adversely affecting the electrochemical performance.[29] Consequently, determining the ideal doped level to optimize electrochemical performance emerges as a critical area of research. Motivated by these findings, the development of advanced TMSe anodes featuring a yolk-shell structure and optimal ion-doped through simple nanostructure engineering and precise ion-doped is a compelling yet challenging objective.

Herein, we have synthesized a Cu^{2+}-doped $Co_{0.85}Se$@N-doped carbon anode (denoted as Cu-$Co_{0.85}Se$@NC-2) for enhancing K^+ storage capacity. The distinctive

yolk-shell structure is engineered to mitigate volume expansion and enhance electrolyte diffusion. Additionally, the introduction of Cu^{2+} introduces a greater number of active sites. Furthermore, the Cu^{2+}-doped not only effectively improves the diffusion and adsorption of K^+, but also enhances the reaction kinetics. As expected, when used as an anode material for PIBs, Cu-$Co_{0.85}Se$@NC-2 exhibits superior rate performance and cycling stability. Most importantly, the pouch cell assembled by coupling the Cu-$Co_{0.85}Se$@NC-2 anode with the Prussian blue (PB) cathode also shows excellent electrochemical performance. The findings of this research are expected to provide a viable and straightforward nanostructure engineering and ion-doped approach to enhance K^+ storage efficiency.

2. Results and discussion

2.1 Theoretical Investigation

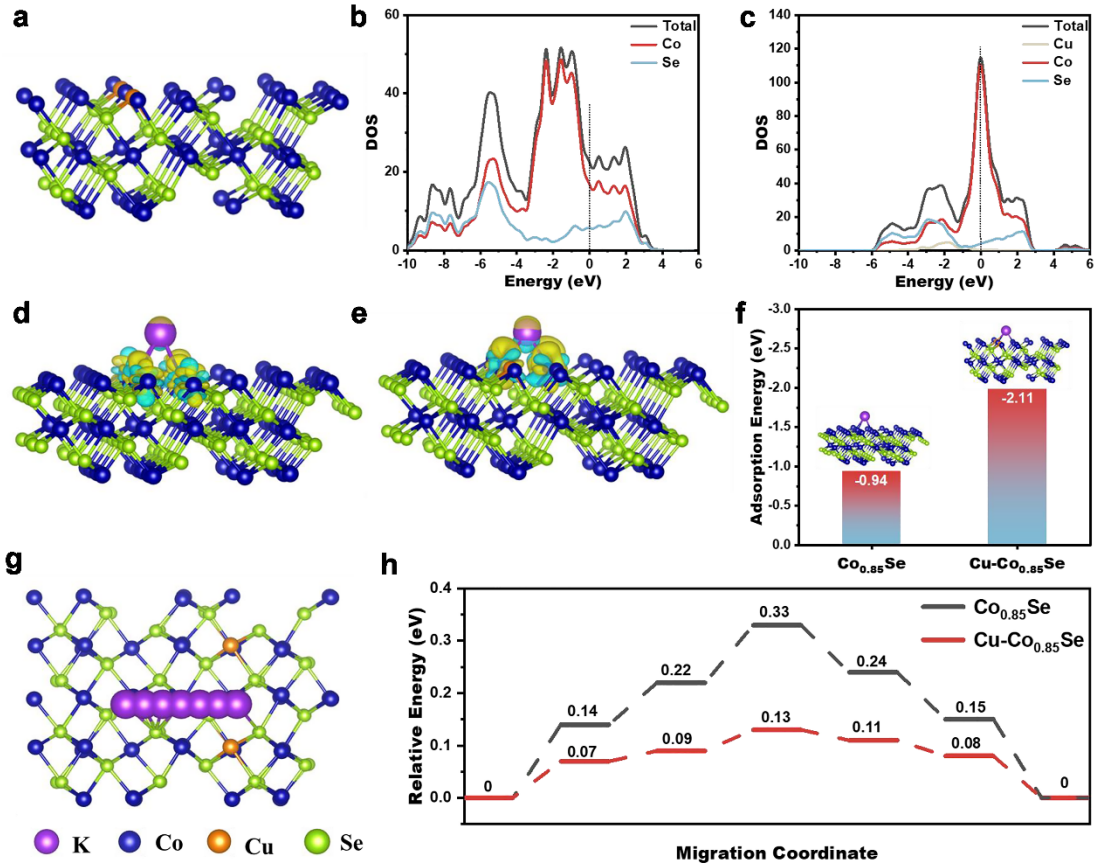

Figure 1. (a) The structural models of Cu-$Co_{0.85}Se$. The density of states (DOS) of (b) $Co_{0.85}Se$ and (c) Cu-$Co_{0.85}Se$. Charge differences of K^+ adsorption in (d) $Co_{0.85}Se$ and (e) Cu-$Co_{0.85}Se$. (f) The adsorption energy of K^+ in $Co_{0.85}Se$ and Cu-$Co_{0.85}Se$. (g) Possible migration pathways for K^+ in Cu-$Co_{0.85}Se$. (h) Calculated K^+ diffusion

barriers in $Co_{0.85}Se$ and Cu-$Co_{0.85}Se$.

DFT calculations were conducted to elucidate the effects of Cu^{2+}-doped on the electronic structure and K^+ storage behavior of $Co_{0.85}Se$. As shown in **Figure 1a** and **Figure S1**, the structural models of $Co_{0.85}Se$ and Cu-$Co_{0.85}Se$ are constructed. The electronic state distribution at the Fermi level for Cu-$Co_{0.85}Se$ is more pronounced (**Figure 1b, c**), indicating that Cu^{2+}-doped effectively modulates the electronic structure and enhances the conductivity, thereby facilitating K^+ storage.[30, 31] **Figure 1d, e** and **Figure S2** illustrate the charge density difference of K^+ adsorbed on $Co_{0.85}Se$ and Cu-$Co_{0.85}Se$, respectively, with cyan and yellow representing electron density accumulation and enrichment. The charg e distribution in Cu-$Co_{0.85}Se$ is more abundant compared to $Co_{0.85}Se$, providing a larger charge concentration distribution for the embedding of K^+.

In addition, the adsorption energy (E_{ads}) of K^+ on $Co_{0.85}Se$ and Cu-$Co_{0.85}Se$ is calculated, with the corresponding adsorption model shown in **Figure 1f**. The E_{ads} value for Cu-$Co_{0.85}Se$ is -2.11 eV, significantly lower than that for $Co_{0.85}Se$ (-0.94 eV), proving that Cu^{2+}-doped is beneficial to the adsorption of K^+. Furthermore, K^+ migration from one of the most stable positions to the adjacent positions is simulated to determine the diffusion energy barrier, and the corresponding model and energy barrier are shown in **Figure g, h** and **Figure S3**. The migration energy barriers of Cu-$Co_{0.85}Se$ are consistently lower than those of $Co_{0.85}Se$. For example, the maximum migration energy barrier for $Co_{0.85}Se$ (0.33 eV) is 2.5 times higher than that for Cu-$Co_{0.85}Se$ (0.13 eV), demonstrating that Cu^{2+}-doped is beneficial to K^+ diffusion and improves rate performance.

2.2 Fabrication and structural analysis

Figure 2a shows the synthesis process of Cu-$Co_{0.85}Se$@NC-*n* (*n*=1, 2 and 3). The preparation of $Co_{0.85}Se$@NC is almost the same as that of Cu-$Co_{0.85}Se$@NC-*n*, except for the addition of Cu^{2+} (see the experimental steps for details). Briefly, ZIF-67@PDA and ZIF-67@PDA-*n* (*n*=1, 2 and 3) samples can be obtained by coating PDA on the surface of ZIF-67, Cu-ZIF-67-1, Cu-ZIF-67-2, and Cu-ZIF-67-3 (**Figure S4**).

Interestingly, the size of the dodecahedron ZIF-67 increases with the increase of Cu^{2+} content. In addition, a critical observation is that upon escalating the $CuSO_4$ concentration to 270 mg, the morphology is destroyed to a certain extent.

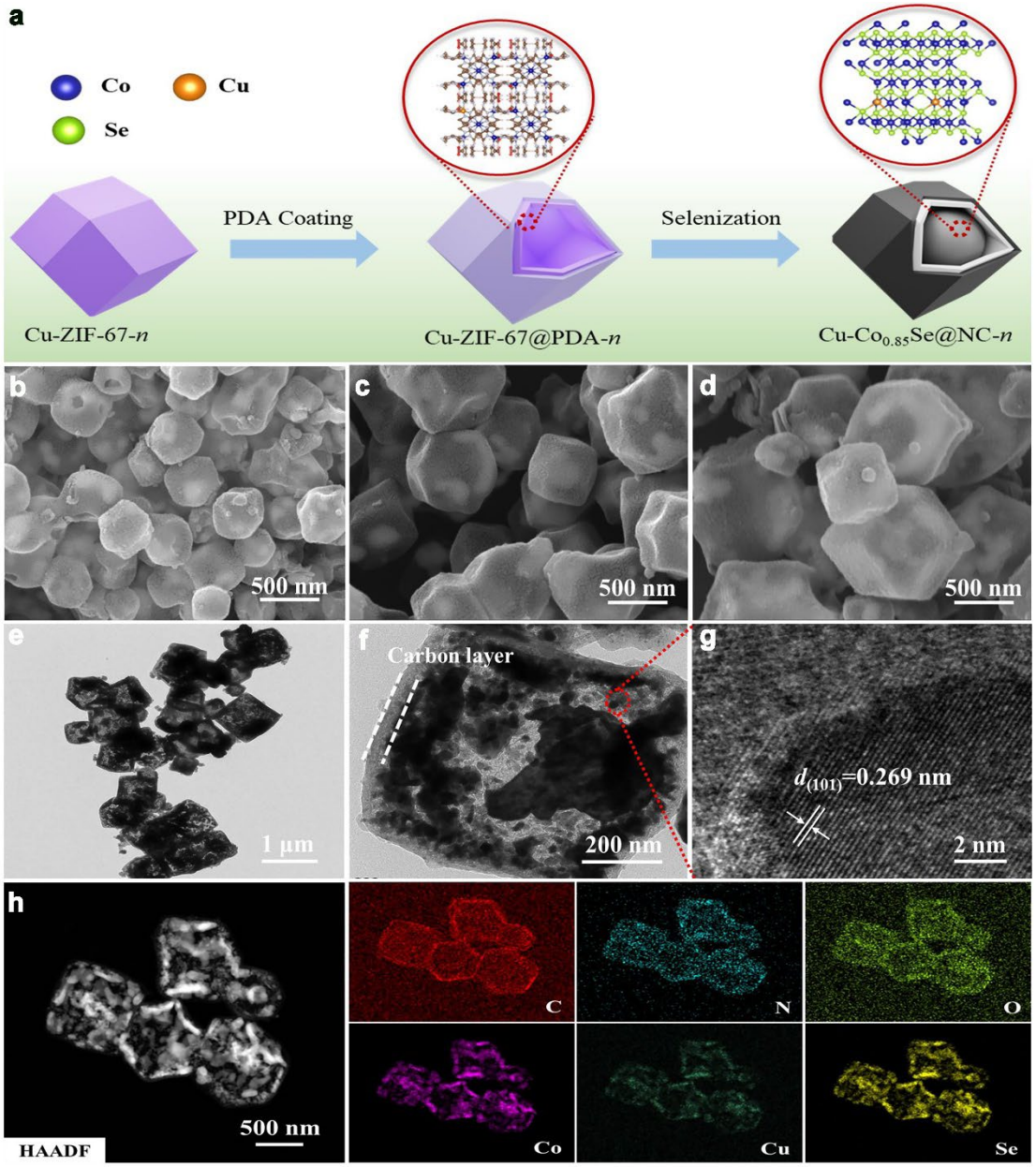

Figure 2. (a) Schematic illustration for the synthesis of the Cu-$Co_{0.85}Se$@NC-*n* nanocomposites. (b-d) SEM images of $Co_{0.85}Se$@NC, Cu-$Co_{0.85}Se$@NC-1, and Cu-$Co_{0.85}Se$@NC-2. (e-g) TEM and HRTEM images of Cu-$Co_{0.85}Se$@NC-2. (h) HAADF-STEM image of Cu-$Co_{0.85}Se$@NC-2 and the elemental distribution of C, N, O, Co, Cu, and Se.

Then, the target sample can be obtained after high-temperature selenization ($Co_{0.85}Se$@NC, Cu-$Co_{0.85}Se$@NC-1, Cu-$Co_{0.85}Se$@NC-2, and Cu-$Co_{0.85}Se$@NC-3), as shown in **Figure 2b-d** and **Figure S5**. The scanning electron microscope (SEM)

morphologies confirm that the samples ($Co_{0.85}Se$@NC, Cu-$Co_{0.85}Se$@NC-1, and Cu-$Co_{0.85}Se$@NC-2) obtained after high-temperature selenization still maintain a dodecahedron and form yolk-shell structure. This structural integrity is advantageous for alleviating volume expansion and enhancing electrolyte diffusion. However, the morphology of Cu-$Co_{0.85}Se$@NC-3 is fragmented, indicating that high-content Cu^{2+}-doped is not conducive to structural maintenance. The transmission electron microscope (TEM) images (**Figure 2e** and **Figure S6**) again confirm the formation of a yolk-shell structure in the synthesized sample, and the yolk exhibits an irregular granular structure. Therefore, Cu^{2+}-doped can simultaneously change the size of the dodecahedron. Nevertheless, excessive Cu^{2+}-doped will destroy the structure, which will affect the performance of the material. These findings suggest that the size and structural integrity of the dodecahedron can be tuned by controlling the Cu^{2+}-doped content, which is conducive to obtaining optimal electrochemical performance.

Figure 2f clearly shows that the PDA-derived carbon layer is evenly wrapped on the surface of the sample with a thickness of about 20 nm. This coating is beneficial to alleviate the volume expansion and improve the cyclic stability of the material. The HRTEM image (**Figure 2g**) reveals a lattice spacing of 0.269 nm for the (101) plane, aligning with the standard d-spacing for $Co_{0.85}Se$ (JCPDS No. 52-1008), thereby confirming the composition of the synthesized sample as $Co_{0.85}Se$.[32] Additionally, high-angle annular dark-field scanning TEM (HAADF-STEM) images presented in **Figure 2h** elucidate the elemental distribution within Cu-$Co_{0.85}Se$@NC-2. The content of Co, Cu, and Se in the yolk is relatively high, indicating that the main component of the yolk is Cu-$Co_{0.85}Se$, and the shell is nitrogen-doped carbon, further proving that the prepared sample is a yolk-shell structure. Furthermore, it also demonstrates that Cu^{2+} is successfully introduced into the sample.

The crystal structure of the above composites was studied through X-ray diffraction (XRD). The XRD patterns of the four samples (**Figure 3a** and **Figure S7**) all show the characteristic diffraction peaks corresponding to $Co_{0.85}Se$ (JCPDS No.52-1008). After the introduction of Cu^{2+}, the strongest diffraction peak shifts to a lower angle,

primarily due to the substitution of the smaller Co atom by the larger Cu atom in $Co_{0.85}Se$.[33, 34] At the same time, the angle of offset increases with the increase of the introduced Cu^{2+}content. However, to unlock the upper limit of the Cu^{2+} content, its introduced content continues to be increased ($CuSO_4$ content increases to 270 mg). It is found that the material underwent phase change and a small amount of Cu_7Se_4 (JCPDS No.26-0557) impurities are formed (**Figure S7**). This result is attributed to the reaction of a large amount of Cu^{2+} with Se, thereby changing the original crystal structure. Consequently, excessive Cu^{2+}-doped not only adversely affects the morphology structure but also leads to the formation of impurities. In light of these findings, subsequent discussions will primarily focus on $Co_{0.85}Se$@NC, Cu-$Co_{0.85}Se$@NC-1, and Cu-$Co_{0.85}Se$@NC-2.

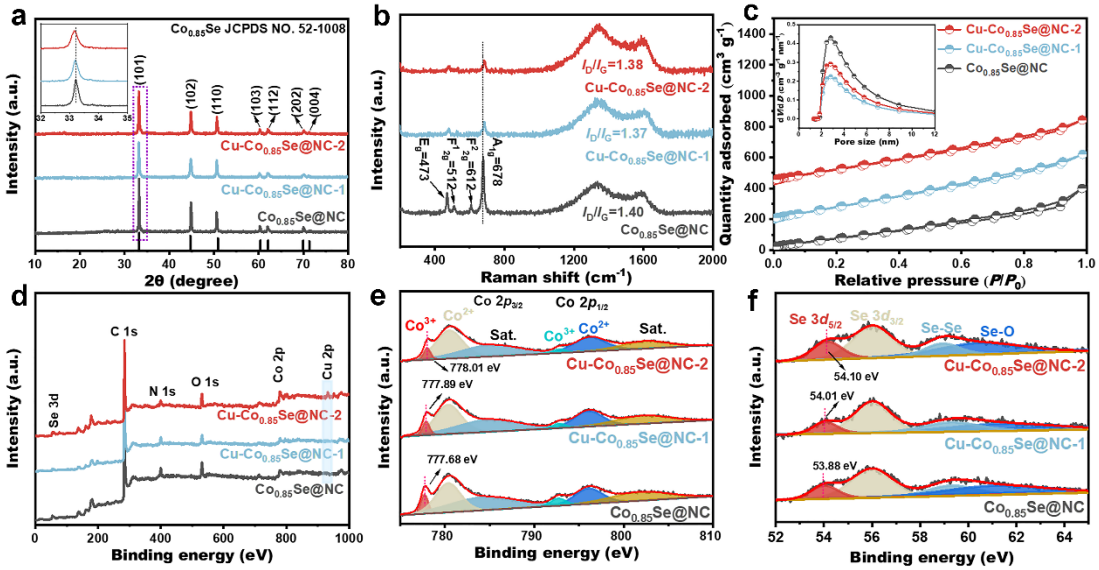

Figure 3. (a) XRD pattern of $Co_{0.85}Se$@NC, Cu-$Co_{0.85}Se$@NC-1, and Cu-$Co_{0.85}Se$@NC-2, respectively. (b) Raman spectra of $Co_{0.85}Se$@NC, Cu-$Co_{0.85}Se$@NC-1, and Cu-$Co_{0.85}Se$@NC-2, respectively. (c) N_2 adsorption-desorption isotherm curves and pore size distribution of $Co_{0.85}Se$@NC, Cu-$Co_{0.85}Se$@NC-1, and Cu-$Co_{0.85}Se$@NC-2, respectively. (d) Full XPS spectra of $Co_{0.85}Se$@NC, Cu-$Co_{0.85}Se$@NC-1, and Cu-$Co_{0.85}Se$@NC-2. High-resolution XPS spectra of (e) Co 2*p* and (f) Se 3*d*.

Raman spectra (**Figure 3b**) were employed to elucidate the structural changes of $Co_{0.85}Se$ after Cu^{2+}-doped. The peak observed at 678 cm^{-1} originates from the A_{1g} mode of CoSe, whereas the peaks at 473, 512, and 612 cm^{-1} represent the E_g, F_{2g}^1, and F_{2g}^2 modes of trivalent cobalt compounds, respectively.[35] The A_{1g} peak slightly shifts

to the right, indicating that Cu^{2+}-doped causes changes in the lattice symmetry of $Co_{0.85}Se$.[26] Additionally, the peaks at 1341 and 1592 cm^{-1} are identified with disordered carbon (D band) and graphitized carbon (G band), respectively. The intensity ratio (I_D/I_G) for $Co_{0.85}Se$@NC, Cu-$Co_{0.85}Se$@NC-1, and Cu-$Co_{0.85}Se$@NC-2 are recorded at 1.40, 1.37, and 1.38, respectively, indicating a relatively low degree of graphitization in the carbon structure.[19] Then, the surface area and pore size distribution of the samples were analyzed using the BET formula ($\frac{1}{V(P_O/P-1)} = \frac{C-1}{V_m \cdot C} \cdot \left(\frac{P}{P_O}\right) + \frac{1}{V_m \cdot C}$ and $S = \frac{V_m N \sigma}{m \times 22400}$), where P and P_O represent the partial pressure and saturated vapor pressure of the adsorbate, respectively; V and V_m are the actual adsorption volume of the sample and the monolayer saturated adsorption volume, respectively; C is a constant related to the adsorption characteristics of the sample; N is Avogadro's constant; σ is the cross-sectional area of a single adsorbate molecule; and m is the mass of the sample.[36] Therefore, the N_2 adsorption/desorption isotherms presented in **Figure 3c** reveal that the materials exhibit similar mesoporous structures with a pore size distribution of about 3 nm. The specific surface area of Cu-$Co_{0.85}Se$@NC-2 (294.0 m^2 g^{-1}) is slightly smaller than Cu-$Co_{0.85}Se$@NC-1 (349.8 m^2 g^{-1}) and $Co_{0.85}Se$@NC (376.7m^2 g^{-1}), which may be conducive to the preparation of dense electrodes and the improvement of energy density, thereby obtaining the best electrochemical performance.[37]

X-ray photoelectron spectroscopy (XPS) was used to further study the valence state and elemental composition of the samples. From the XPS spectra (**Figure 3d**), it can be seen that the signal peaks of C, N, O, Se, and Co are detected in all samples. Additionally, a weak Cu signal peak can be detected, proving the successful introduction of Cu^{2+} (**Figure 3d** and **Figure S8**). **Figure S9** shows the C 1*s* and N 1*s* spectra of Cu-$Co_{0.85}Se$@NC-2. Among them, the C 1*s* spectrum can be deconvoluted into four peaks, which correspond to C-C (~284.52 eV), C-N (~285.30 eV), C-O (~286.47 eV), and C=O (~289.69 eV), respectively. Three peaks are observed in the N 1*s* spectrum, corresponding to pyridine N (~398.55 eV), pyridine N (~400.23 eV), and oxide N (~402.24 eV).[38] To be noted, the presence of C-N bonds means the existence

of the N-doped, which is beneficial to promote the electron/ion transfer efficiency, thereby improving the conductivity.[39] For the Co 2*p* spectrum of $Co_{0.85}Se$@NC (**Figure 3e**), two peaks at ~777.68 and ~793.65 eV can be attributed to Co^{3+}, while the peaks at ~780.45 and ~796.36 eV are related to Co^{2+}. Two shake-up satellites located at ~784.98 and ~802.20 eV correspond to antibonding orbits between Se and Co atoms.[18, 40] As the Cu^{2+}-doped content increases, the 2*p* peak of Co shifts slightly toward a higher binding energy, indicating that the electronic structure of Co changes.[26, 28] The Se 3*d* spectra (**Figure 3f**) exhibit four characteristic peaks of Se $3d_{5/2}$ (~53.88 eV), Se $3d_{3/2}$ (~55.94 eV), Se-Se bonds (~58.92 eV) and Se-O bonds (~60.53 eV), respectively.[17, 41] Interestingly, Se 3*d* spectra also shift toward higher binding energies, verifying that Cu^{2+}-doped induces electron density changes on Co. In addition, the relative contents of Cu and Co in the samples were determined by inductively coupled plasma optical emission spectrometry. The results shows that the Cu/Co atomic ratios of Cu-$Co_{0.85}Se$@NC-1 and Cu-$Co_{0.85}Se$@NC-2 samples are about 0.03 and 0.07, respectively (**Table S1**).

2.3 Potassium storage performance

The potassium storage performance was assessed by assembling CR2032 coin cells with a voltage range of 0.01-3 V. **Figure 4a** and **Figure S10a** present the rate performance of $Co_{0.85}Se$@NC, Cu-$Co_{0.85}Se$@NC-1, Cu-$Co_{0.85}Se$@NC-2 and Cu-$Co_{0.85}Se$@NC-3. Notably, the Cu-$Co_{0.85}Se$@NC-2 electrode exhibits the best rate performance. At current densities ranging from 0.1 to 10 A g^{-1}, the reversible specific capacities are 357.8, 383.9, 349.5, 336.8, 312.4, 288.2, 255.6 and 208.1 mAh g^{-1}, respectively. Upon returning to a current density of 0.1 A g^{-1}, the reversible specific capacity remains at 423.5 mAh g^{-1}, demonstrating excellent reversibility and structural stability. The slightly higher capacity compared to the initial value may be attributed to the reduced resistance of the electrode material following cycling, resulting from electrochemical activation.[42] Clearly, Cu^{2+}-doped enhances specific capacity and rate performance. However, with increased Cu^{2+}-doped content, the rate performance of the Cu-$Co_{0.85}Se$@NC-3 electrode is not satisfactory, likely due to

structural damage from excessive ion-doped, as confirmed by SEM and TEM analyses. Thus, an optimal Cu^{2+}-doped level is necessary to achieve the best rate performance. Additionally, compared to other reported TMSe anodes for PIBs (**Figure 4b**), Cu-$Co_{0.85}Se$@NC-2 exhibits outstanding rate performance.[12, 15, 20, 26, 43-47]

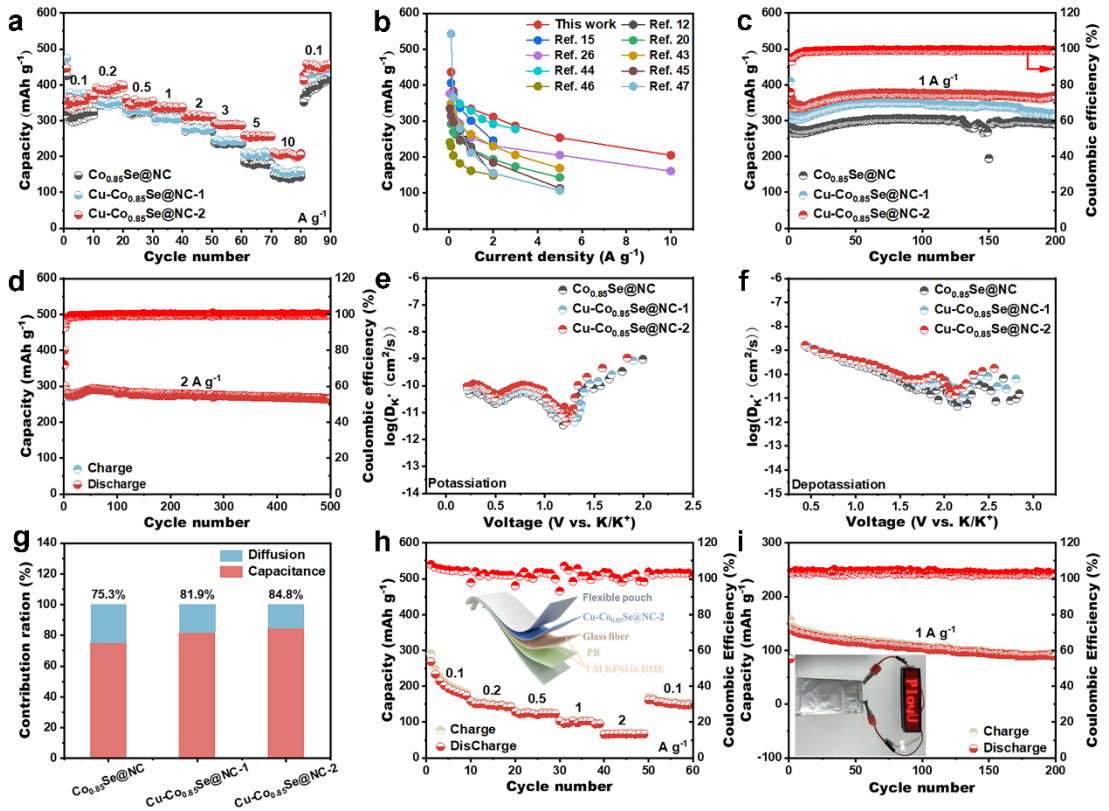

Figure 4. (a) Rate performances of $Co_{0.85}Se$@NC, Cu-$Co_{0.85}Se$@NC-1, and Cu-$Co_{0.85}Se$@NC-2, respectively. (b) Comparison of the rate performance of Cu-$Co_{0.85}Se$@NC-2 with other literature. (c) Cycling performances of $Co_{0.85}Se$@NC, Cu-$Co_{0.85}Se$@NC-1 and Cu-$Co_{0.85}Se$@NC-2 at 1 A g^{-1}. (d) Long-cycling performance of Cu-$Co_{0.85}Se$@NC-2 at 2 A g^{-1}. (e, f) Diffusion coefficients were calculated from the GITT potential profiles during potassiation/depotassiation. (g) Ratio of capacitive contribution of $Co_{0.85}Se$@NC, Cu-$Co_{0.85}Se$@NC-1 and Cu-$Co_{0.85}Se$@NC-2 at 1.0 mV s^{-1}. (h) Rate performance of Cu-$Co_{0.85}Se$@NC-2//PB pouch cell (the inserted picture is the schematic diagram of pouch cell). (i) Long-term cycling performance of Cu-$Co_{0.85}Se$@NC-2//PB pouch cell at a current density of 1 A g^{-1} (the inserted picture shows the working status of the pouch cell).

Figure S11 presents the initial charge/discharge curves of $Co_{0.85}Se$@NC, Cu-$Co_{0.85}Se$@NC-1, and Cu-$Co_{0.85}Se$@NC-2 electrodes at a current density of 0.2 A g^{-1}. The charge and discharge specific capacities of Cu-$Co_{0.85}Se$@NC-2 are 404.1 and 507.9 mAh g^{-1}, respectively. Its initial Coulombic efficiency (ICE) is ~79.6%,

surpassing those of $Co_{0.85}Se$@NC (~61.7%) and Cu-$Co_{0.85}Se$@NC-1 (~75.3%). The improved ICE for Cu-$Co_{0.85}Se$@NC-2 can be attributed to the improved reversibility of the potassiation/depotassiation process, resulting from the optimal Cu^{2+}-doped and the yolk-shell structure with a lower specific surface area.[16, 48, 49] The cycling performance at a current density of 0.2 A g^{-1} is depicted in **Figure S12**. After 200 cycles, the Cu-$Co_{0.85}Se$@NC-2 electrode maintains the highest reversible specific capacity of 432.5 mAh g^{-1}, with a CE approaching 100%, indicating good cycling stability at low current density. The cycling stability of the electrodes at a current density of 1 A g^{-1} is shown in **Figure 4c** and **Figure S10b**, where the Cu-$Co_{0.85}Se$@NC-2 electrode also demonstrates the highest reversible specific capacity and nearly 100% CE after 200 cycles. Even at a high current density of 2 A g^{-1} (**Figure 4d**), the reversible specific capacities remain at 239.7 mAh g^{-1} after 500 cycles, with a capacity retention rate of 80.4%, demonstrating excellent cycling durability. Notably, the specific capacities initially decrease and then gradually increase and stabilize during the cycling process, possibly due to the rapid loss of K^+ mobility or the increased amount of K^+ escaping from the electrode lattice.[50] Furthermore, the TEM image (**Figure S13**) clearly shows that the yolk-shell structure of the Cu-$Co_{0.85}Se$@NC-2 electrode remains intact after 50 cycles at 1 A g^{-1}, which fully proves the yolk-shell structure effectively alleviates volume expansion and supports its excellent cycling stability. Compared to recently reported TMSe anodic material (**Table S2**), the Cu-$Co_{0.85}Se$@NC-2 electrode also exhibits superior rate performance and cycling stability, making it a promising candidate for potential applications as an anodic material.

The reaction kinetics of the material were evaluated using electrochemical impendence spectra (EIS) testing **(Figure S14**). The impedance values fitted by the equivalent circuit model indicate that the Cu-$Co_{0.85}Se$@NC-3 electrode exhibits the lowest impedance, followed by Cu-$Co_{0.85}Se$@NC-2, suggesting that higher Cu^{2+}-doped content enhances the material's conductivity (**Table S3**). However, excessive doped content leads to structural collapse, the rate performance and cycling stability

are not ideal. Therefore, an optimal Cu^{2+}-doped content is crucial to maintaining the material structure while achieving the best electrochemical performance. In addition, to elucidate the role of the introduction of Cu^{2+} in improving K^+ kinetics, the galvanostatic intermittent titration technique (GITT) was used, as described by the following formula: $D_{K^+} = \frac{4}{\pi\tau}\left(\frac{m_B V_M}{M_B S}\right)^2 (\frac{\triangle E_S}{\triangle E_\tau})^2$.[2] Where τ represents the duration time of the current pulse; m_B and V_M represent the mass of the active materials and the molar volume of the samples, respectively; M_B and S are the molecular weight and the total surface electrode in contact with the electrolyte, respectively; $\triangle E_S$ and $\triangle E_\tau$ are the change of steady-state voltage for the corresponding step and the potential difference during the current pulse, respectively. During the whole charge-discharge process, the K^+ diffusion coefficient of the Cu-$Co_{0.85}Se$@NC-2 electrode (during the potassiation process varies from 1.21×10^{-11} to 1.83×10^{-9} cm^2 s^{-1}) is significantly higher than that of the Cu-$Co_{0.85}Se$@NC-1 and $Co_{0.85}Se$@NC electrodes (**Figure 4e, f** and **Figure S15**). These results prove that Cu^{2+}-doped helps to improve K^+ diffusion, thereby resulting in excellent rate performance.

Since the Cu-$Co_{0.85}Se$@NC-2 electrode has excellent electrochemical performance, its capacitive characteristics were investigated. **Figure S16a** shows the cyclic voltammetry (CV) curve of the Cu-$Co_{0.85}Se$@NC-2 electrode within a scan range of 0.2-1.0 mV s^{-1}. The electrochemical storage process of CV data at different scan rates is analyzed through the power law equation ($i = av^b$). Among them, a, b, and v are adjustable parameters and scan rate, respectively.[51] As shown in **Figure S16b**, the b values of all anode and cathode peaks range between 0.5 and 1.0, proving that the Cu-$Co_{0.85}Se$@NC-2 electrode exhibits both pseudo-capacitance and diffusion process mechanisms. The contribution ratio of pseudo-capacitance can be obtained from the following formula: $i(V) = k_1 v + k_2 v^{1/2}$, where $k_1 v$ and $k_2 v^{1/2}$ represent the contributions of pseudo-capacitance and diffusion-controlled capacitance, respectively.[52] **Figure 4g** and **Figure S17** clearly show that when the scan rate is 1.0 mV s^{-1}, the pseudo-capacitance contribution rate of the Cu-$Co_{0.85}Se$@NC-2 electrode (84.8%) is higher than that of $Co_{0.85}Se$@NC (75.3%) and Cu-$Co_{0.85}Se$@NC-1 (81.9%).

Moreover, at scan rates are 0.2, 0.4, 0.6, 0.8, and 1.0 mV s^{-1}, the capacitance control contributions of Cu-$Co_{0.85}$Se@NC-2 are 66.3%, 70.0%, 75.3%, 80.1% and 84.8%, respectively (**Figure S18**). Obviously, as the scan rate increases, the capacitive contribution gradually increases, indicating that the pseudo-capacitance behavior plays a dominant role in the electrochemical reaction, ensuring ultrafast K^+ transport kinetics during the potassiation/depotassiation process.

Given the exceptional electrochemical performance and practical applicability of the Cu-$Co_{0.85}$Se@NC-2 electrode, a pouch cell was assembled using the activated Cu-$Co_{0.85}$Se@NC-2 anode and a PB cathode, with an electrolyte of 1 M KFSI in DME (the schematic diagram of the pouch cell is shown in the inset of **Figure 4h**). As illustrated in **Figure 4h**, when the current density increases from 0.1 to 2 A g^{-1}, the reversible specific capacities of the Cu-$Co_{0.85}$Se@NC-2//PB pouch cell are 203.5, 149.5, 124, 104.5, and 67.1 mAh g^{-1}, respectively. The specific capacity and current density are calculated based on the anodic active material, with a voltage window range of 0.5-3.6 V. When the current density returns to 0.1 A g^{-1}, the specific capacity also returns to 161.4 mAh g^{-1}, indicating excellent rate performance and good reversibility of the Cu-$Co_{0.85}$Se@NC-2//PB pouch cell. The rate performance trends at 0.1 and 0.2 A g^{-1} in **Figure 4h** and **Figure 4a** are slightly different, possibly due to the fact that the Cu-$Co_{0.85}$Se@NC-2 electrode is fully activated before assembling the pouch cell but not in the half-cell.[42, 53] Furthermore, at a current density of 1 A g^{-1} (**Figure 4i**), the specific capacity of the Cu-$Co_{0.85}$Se@NC-2//PB pouch cell can be maintained at 92.8 mAh g^{-1} after 200 cycles, with a specific capacity retention rate of up to 68%. In addition, the pouch cell is capable of powering LEDs. Therefore, Cu-$Co_{0.85}$Se@NC-2 is a promising electrode material for energy storage applications.

2.4 Reaction mechanism

The phase evolution and K^+ storage mechanism of Cu-$Co_{0.85}$Se@NC-2 were studied using the first three CV curves, ex-situ XRD, ex-situ XPS, and ex-situ TEM. **Figure S19** shows the first three cycle CV curves of the Cu-$Co_{0.85}$Se@NC-2 electrode at a scan rate of 0.2 mV s^{-1}. During the initial cathodic scan, the reduction peak located at

0.91 V is attributed to the insertion of K^+ into $Co_{0.85}Se$. Concurrently, a peak at 0.62 V corresponds to the conversion reaction of $Co_{0.85}Se$ to Co and potassium selenide species, as well as the formation of the solid electrolyte interface (SEI) film during the initial potassiation.[18, 19] In contrast, during the anodic scan, the oxidation peaks at 1.71 V and 2.03 V are associated with the formation of Cu-$K_xCo_{0.85}Se$ from Co, Cu, and K_2Se, and the subsequent recovery to Cu-$Co_{0.85}Se$, respectively. The overlap of the CV curves in the second and third scans indicates good cycling stability.[54]

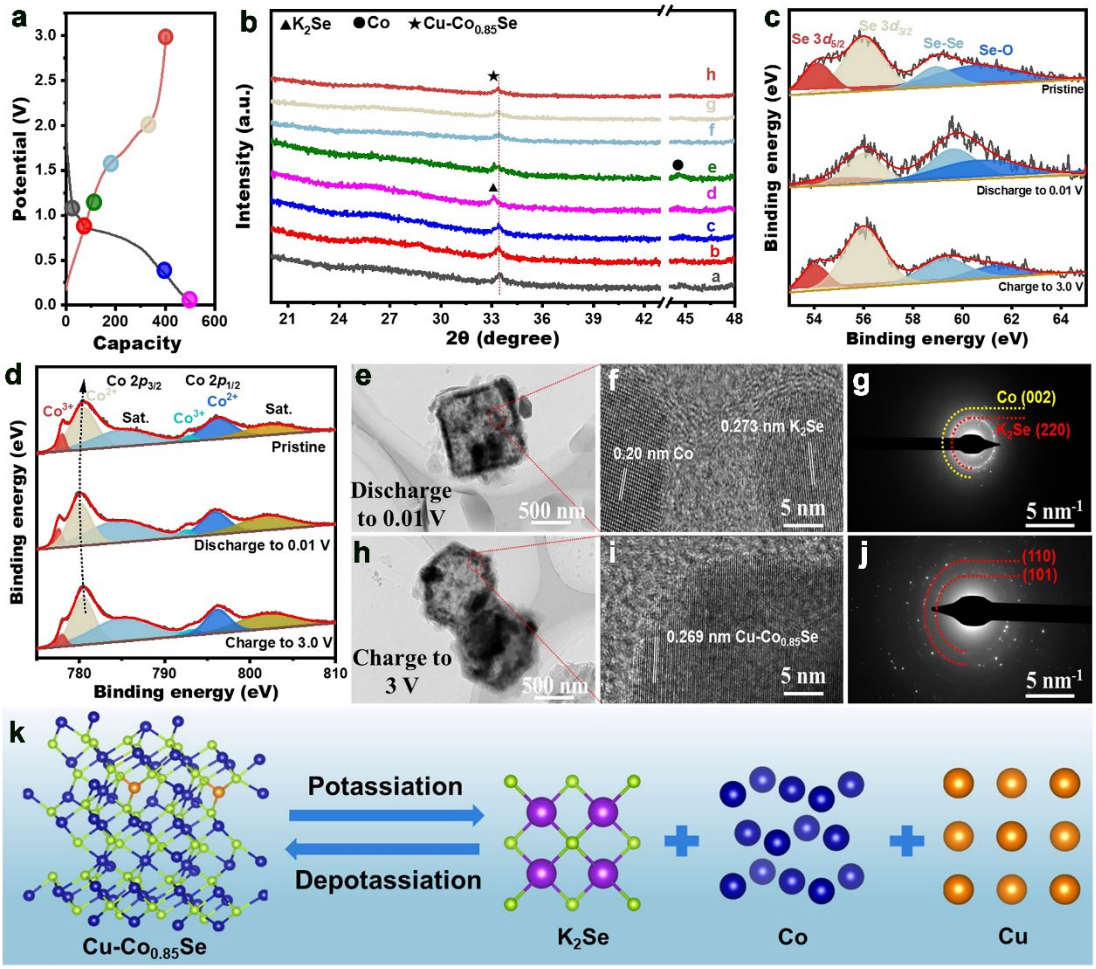

Figure 5. (a,b) Ex-situ XRD patterns of Cu-$Co_{0.85}Se$@NC-2 at different voltage states at 0.1 A g^{-1}. (c,d) The corresponding ex-situ XPS spectra of Se 3*d* and Co 2*p* (d). (e-j) TEM, HRTEM, and corresponding selected area diffraction (SAED) pattern of Cu-$Co_{0.85}Se$@NC-2 at different states. (k) Schematic illustration of the reaction mechanism.

For the ex-situ XRD patterns (**Figure 5a, b**) during the first discharge process, the intensity of the (101) plane gradually decreases and eventually disappears as K^+ is inserted from open circuit voltage to 0.01 V. Subsequently, the characteristic peaks of

K_2Se (220) (JCPDS card No. 47-1703) and Co (002) (JCPDS Card No. 05-0727) appear, indicating that Cu-$Co_{0.85}Se$ undergoes a conversion reaction at this voltage stage, which is completed at 0.01 V. During the charging process up to 3.0 V, the characteristic peaks of K_2Se and Co disappear, and the characteristic peaks of (101) plane reappear, demonstrating that this reaction is highly reversible. The ex-situ XRD results are in good agreement with the above CV. Notably, no characteristic peak of Cu is detected, likely due to the low content of the introduced Cu element, rendering its peak intensity too low to be detected.

Ex-situ XPS analysis of the Cu-$Co_{0.85}Se$@NC-2 anode was performed under different charge and discharge states. The Se 3*d* spectra of the pristine electrode have two peaks at ~53.88 and ~55.94 eV, corresponding to Se $3d_{5/2}$ and Se $3d_{3/2}$ orbitals, respectively. When discharge to 0.01 V (**Figure 5c**), these peaks shifted to ~54.25 and 56.04 eV, respectively, indicating the formation of K-Se bonds.[55, 56] Upon recharge to 3.0 V, the two peaks returned to their original positions. In addition, the characteristic peak intensity of Se 3*d* spectra decreases during the discharge process and recovers during the charging process, suggesting that the Cu-$Co_{0.85}Se$@NC-2 electrode undergoes a highly reversible conversion reaction.[12] The Co 2*p* peaks (**Figure 5d**) shift to lower binding energies upon full discharge, corresponding to the formation of metallic Co, and revert back upon full charge, indicating the reformation of $Co_{0.85}Se$.[18] Similarly, the Cu 2*p* spectrum (**Figure S20**) shifts to lower energy levels when fully discharged to 0.01 V, corresponding to the reduction of doped Cu^{2+}. When restored to 3 V, the peak of Cu 2*p* returns to its original binding energy, indicating that Cu^{2+} is re-doped into $Co_{0.85}Se$ in the Cu-$Co_{0.85}Se$@NC-2 anode with high reversibility.[28, 57] Furthermore, ex-situ TEM was used to examine the morphology and phase evolution of Cu-$Co_{0.85}Se$@NC-2. The Cu-$Co_{0.85}Se$ yolk remains enclosed within the carbon shell when fully discharged to 0.01 V or charged to 3 V, as shown in **Figure 5e**. The HRTEM image and SAED pattern (**Figure 5f, g**) reveal the lattice fringes with an interlayer spacing of 0.20 and 0.273 nm, corresponding to the (002) plane of Co and the (220) plane of K_2Se, respectively. When recharged to 3.0 V

(**Figure 5h**), the morphology remains intact, indicating that the yolk-shell structure is beneficial to alleviate the volume change caused by charging and discharging. The corresponding lattice fringes and SAED patterns in **Figure 5i, j** correspond to $Co_{0.85}Se$, consistent with the ex-situ XRD results. These findings demonstrate that Cu-$Co_{0.85}Se$@NC-2 exhibits high reversibility and structural stability during K^+ storage. Therefore, the K^+ storage reaction mechanism of the Cu-$Co_{0.85}Se$@NC-2 anode is elucidated as follows (illustrated in **Figure 5k**).

$$Cu - Co_{0.85}Se + 2K^+ + 2e^- \rightarrow K_2Se + 0.85Co + Cu \quad \text{(potassiation)}$$

$$K_2Se + 0.85Co + Cu \rightarrow Cu - Co_{0.85}Se + 2K^+ + 2e^- \quad \text{(depotassiation)}$$

3. Conclusion

In this work, we have successfully prepared the Cu-$Co_{0.85}Se$@NC-2 anode with a yolk-shell structure through nanostructure engineering and ion-doped, highlighting the advantage of Cu^{2+}-doped in facilitating rapid diffusion of K^+. In addition, the yolk-shell structure effectively alleviates the volume change. Benefiting from the construction of yolk-shell structure and optimal concentration of Cu^{2+}-doped, Cu-$Co_{0.85}Se$@NC-2 demonstrates excellent rate performance (208.1 mA h g^{-1} at 10 A g^{-1}) and cycling stability (239.7 mA h g^{-1} at 2 A g^{-1} after 500 cycles). Furthermore, the Cu-$Co_{0.85}Se$@NC-2//PB pouch cell also shows outstanding rate performance (67.1 mAh g^{-1} at 2 A g^{-1}) and cyclability (92.8 mAh g^{-1} after 200 cycles at 1 A g^{-1}). Our strategy can be extended to other TMCs, providing a simple and effective approach for developing high-rate and stable anode materials for PIBs.

4. Experiment

4.1 Preparation of Cu^{2+}-doped $Co_{0.85}Se$@N-doped carbon (Cu-$Co_{0.85}Se$@NC)

Firstly, according to our previous work,[58] 3.2 g $Co(NO_3)_2 \cdot 6H_2O$ and $CuSO_4$ (the mass was 0, 90, 180, and 270 mg, respectively) were dissolved in 180 mL methanol (named as solution A). Then, 4 g 2-methylimidazole was dissolved in 90 mL methanol (named solution B). Immediately afterward, solution B was quickly added to solution A stirred for 10 minutes, and then stood still for 24 hours. The precursors obtained by

centrifugation and vacuum drying were named ZIF-67, Cu-ZIF-67-1, Cu-ZIF-67-2, and Cu-ZIF-67-3, respectively.

Then, 300 mg of the above-mentioned precursors were respectively dispersed in 200 mL tri-butter solution (0.1 M, solvent is ethanol), followed by dropwise addition of 20 mL ethanol solution (150 mg dopamine) with constant stirring. The obtained mixed solution was placed at room temperature for 24 hours. ZIF-67@PDA and Cu-ZIF-67@PDA-*n* (*n*=1, 2, and 3) samples can be obtained by centrifugation and vacuum drying.

Finally, the above samples (ZIF-67@PDA and Cu-ZIF-67@PDA-*n*) and selenium powder (the mass ratio was 1:2) were calcined at 800 ℃ for 2 hours (the heating rate was 2 ℃ min^{-1}, Ar/H_2 mixed atmosphere), and the obtained products were named $Co_{0.85}Se$@NC, Cu-$Co_{0.85}Se$@NC-1, Cu-$Co_{0.85}Se$@NC-2, and Cu-$Co_{0.85}Se$@NC-3, respectively.

4.2 Characterization

The morphology and microstructure of all synthesized materials were examined using a SEM (Navo Nano SEM450) and a TEM (Talos F200X). The crystalline phase of the samples was determined by XRD (Rigaku SmartLab 9kW-Advance). Raman spectroscopy (Thermo Fisher) was conducted using a He-Ne laser (532 nm). The surface area and pore size distribution of the samples were analyzed with an Autosorb-IQ2 Brunauer-Emmett-Teller (BET) analyzer. The chemical states were identified through XPS (Thermo Fisher Scientific 250Xi) using Al Kα radiation as the X-ray source.

4.3 Electrochemical measurements

For the half-cell test, the active materials ($Co_{0.85}Se$@NC, Cu-$Co_{0.85}Se$@NC-1, Cu-$Co_{0.85}Se$@NC-2, and Cu-$Co_{0.85}Se$@NC-3), biochar,[59] and Polyvinylidene fluoride (PVDF) binder were mixed in N-methyl-2-pyrolidone (NMP) at a mass ratio of 8:1:1 to prepare the working electrode. The prepared slurry was uniformly coated on the copper foil and dried under vacuum at 100 ℃ for 12 hours. These electrodes were then punched into discs with a diameter of 12 mm (mass loading was ~1.5 mg per

electrode). The coin cells (CR2023) were assembled in glove box (Ar-filled) with glass fiber (Whatman) and potassium foil served as separators and counter electrodes, and the electrolyte was 1 M potassium bis(fluorosulfonyl)imide (KFSI) in dimethoxyethane (DME). As for the pouch battery assembly, the activated Cu-$Co_{0.85}Se$@NC-2 (Cu-$Co_{0.85}Se$@NC-2 was activated after 10 cycles at a current density of 0.1 A g^{-1} in the half-cell) and Prussian blue ($K_{0.72}Fe[Fe(CN)_6]$, PB)[60] served as the anode and cathode, respectively. The electrochemical performance was evaluated using a battery test system with a voltage window of 0.01 to 3.0 V. The CV curves (the scanning rate is 0.2-1.0 mV s^{-1}) and EIS measurements were conducted using a CHI-760 electrochemical workstation (Chenhua, Shanghai, China).

4.4 Theoretical Calculations

Density functional theory (DFT) calculations were performed using the VASP code. The Perdew-Burke-Ernzerhof (PBE) functional within generalized gradient approximation (GGA) was employed to handle the exchange-correlation, while the projector augmented-wave pseudopotential (PAW) was utilized with a kinetic energy cut-off of 500 eV to describe the expansion of the electronic eigenfunctions. The Brillouin-zone integration was sampled by a Γ-centered 7 × 7 × 1 Monkhorst-Pack k-point. All atomic positions were fully relaxed until the energy and force converged to the tolerance of 1 × 10^{-6} eV and 0.01 eV/Å, respectively. The dispersion-corrected DFT-D method was applied to account for long-range interactions. The climbing image nudged elastic band method (CI-NEB) was used to compute the minimum energy pathway of the reaction and its corresponding activation barrier. The adsorption energy (E_{ads}) of a complex formed between Cu-$Co_{0.85}Se$ and K was calculated using the following equation: $E_{ads} = E_{\mathrm{complex}} - (E_{\mathrm{Cu}-Co_{0.85}Se} + E_{\mathrm{K}})$, Where E_{complex} is the total energy of the molecular complex of Cu-$Co_{0.85}Se$ and K. $E_{\mathrm{Cu}-Co_{0.85}Se}$ and E_{K} are the total energies of isolated molecules Cu-$Co_{0.85}Se$ and K, respectively.

Supporting Information

Supporting Information is available from the Wiley Online Library or from the author.

Acknowledgment

The authors gratefully acknowledge financial support from the PolyU Postdoc Matching Fund 1-W34P, ITF project ITP/023/22TP, PolyU RCRE fund 1-BBCB, and IWEAR fund 1-CD8E.

Conflict of Interest

The authors declare no conflict of interest.

References

[1] E.C. Evarts, Nature **2015**, 526, S93-S95.

[2] M. Han, J. Liu, C. Deng, J. Guo, Y. Mu, Z. Zou, K. Zheng, F. Yu, Q. Li, L. Wei, L. Zeng, T. Zhao, Adv. Energy Mater. **2024**, 14, 2400246.

[3] Y. Xu, Y. Du, H. Chen, J. Chen, T. Ding, D. Sun, D.H. Kim, Z. Lin, X. Zhou, Chem. Soc. Rev. **2024**, 53, 7202-7298.

[4] H. Deng, L. Wang, S. Li, M. Zhang, T. Wang, J. Zhou, M. Chen, S. Chen, J. Cao, Q. Zhang, J. Zhu, B. Lu, Adv. Funct. Mater. **2021**, 31, 2107246.

[5] Y. Liu, X. Hu, J. Li, G. Zhong, J. Yuan, H. Zhan, Y. Tang, Z. Wen, Nat. Commun. **2022**, 13, 663.

[6] N. Hussain, M. Li, B. Tian, H. Wang, Adv. Mater. **2021**, 33, e2102164.

[7] J.-Y. Hwang, H.M. Kim, C.S. Yoon, Y.-K. Sun, ACS Energy Lett. **2018**, 3, 540-541.

[8] J. Zhou, Y. Liu, S. Zhang, T. Zhou, Z. Guo, InfoMat **2020**, 2, 437-465.

[9] M. Ma, S. Chong, K. Yao, H.K. Liu, S.X. Dou, W. Huang, Matter **2023**, 6, 3220-3273.

[10] H. Zhang, Y. Cheng, Q. Zhang, W. Ye, X. Yu, M.S. Wang, ACS Nano **2021**, 15, 10107-10118.

[11] K. Sada, J. Darga, A. Manthiram, Adv. Energy Mater. **2023**, 13, 2302321.

[12] W. Feng, X. Wei, F. Cao, Y. Li, X. Zhang, Y. Li, W. Liu, J. Han, D. Kong, L. Zhi, Energy Storage Mater. **2024**, 65, 103186.

[13] C. Lamiel, I. Hussain, H. Rabiee, O.R. Ogunsakin, K. Zhang, Coordin. Chem. Rev. **2023**, 480, 215030.

[14] Q. Yun, L. Li, Z. Hu, Q. Lu, B. Chen, H. Zhang, Adv. Mater. **2020**, 32, e1903826.

[15] Y. Liu, Q. Deng, Y. Li, Y. Li, W. Zhong, J. Hu, X. Ji, C. Yang, Z. Lin, K. Huang, ACS Nano **2021**, 15, 1121-1132.

[16] Y. Liu, M. Qiu, X. Hu, J. Yuan, W. Liao, L. Sheng, Y. Chen, Y. Wu, H. Zhan, Z. Wen, Nano-Micro Lett. **2023**, 15, 104.

[17] D. Chen, Y. Liu, P. Feng, X. Tao, Z. Huang, X. Zhang, M. Zhou, J. Chen, J. Energy Chem. **2024**, 91, 111-121.

[18] W.W. Shen, Y.Y. Hsieh, H.Y. Tuan, J. Colloid. Interf. Sci. **2023**, 643, 626-639.

[19] C. Atangana Etogo, H. Huang, H. Hong, G. Liu, L. Zhang, Energy Storage Mater. **2020**, 24, 167-176.

[20] N. Ren, L. Wang, J. Dong, K. Cao, Y. Li, F. Chen, J. Xiao, B. Pan, C. Chen, Chem. Eng. J. **2023**, 458, 141489.

[21] Y. Yin, Y. Zhang, N. Liu, L. Fan, N. Zhang, Energy Environ. Mater. **2020**, 3, 529-534.

[22] X.F. Lu, Y. Fang, D. Luan, X.W.D. Lou, Nano Lett. **2021**, 21, 1555-1565.

[23] W. Yang, J. Wang, J. Jian, Energy Storage Mater. **2024**, 66, 103249.
[24] J. Feng, S.-h. Luo, S.-x. Yan, Y. Zhan, Q. Wang, Y.-h. Zhang, X. Liu, L.-j. Chang, Small **2021**, 17, 2101887.
[25] D. Chen, S. Sun, G. Yu, L. Qin, W. Wang, M. Jiang, J. Chen, Carbon **2020**, 166, 91-100.
[26] H. Shan, J. Qin, J. Wang, H.M.K. Sari, L. Lei, W. Xiao, W. Li, C. Xie, H. Yang, Y. Luo, G. Zhang, X. Li, Adv. Sci. (Weinh) **2022**, 9, e2200341.
[27] B. Chen, D. Chao, E. Liu, M. Jaroniec, N. Zhao, S.-Z. Qiao, Energy Environ.l Sci. **2020**, 13, 1096-1131.
[28] Y. Dou, C.T. He, L. Zhang, H. Yin, M. Al-Mamun, J. Ma, H. Zhao, Nat. Commun. **2020**, 11, 1664.
[29] W. Zhang, Z. Cao, W. Wang, E. Alhajji, A.H. Emwas, P. Costa, L. Cavallo, H.N. Alshareef, Angew. Chem. Int. Ed. **2020**, 59, 4448-4455.
[30] L. Pan, R. Hu, Y. Zhang, D. Sha, X. Cao, Z. Li, Y. Zhao, J. Ding, Y. Wang, Z. Sun, Nano-Micro Lett. **2023**, 15, 225.
[31] X. Zhao, F. Zhang, H. Li, H. Dong, C. Yan, C. Meng, Y. Sang, H. Liu, Y.-G. Guo, S. Wang, Energy Environ. Sci. **2024**, 17, 3629-3640.
[32] Z. Liu, K. Han, P. Li, W. Wang, D. He, Q. Tan, L. Wang, Y. Li, M. Qin, X. Qu, Nano-Micro Lett. **2019**, 11, 96.
[33] Y. Li, M. Chen, B. Liu, Y. Zhang, X. Liang, X. Xia, Adv. Energy Mater. **2020**, 10, 2000927.
[34] L. Hu, P. Zhong, J. Zhu, J. Wang, Y. Zheng, X. Lin, Y. Zhang, H. Yang, CrystEngComm **2024**, 26, 4804-4811.
[35] Y. Huang, Z. Wang, Y. Jiang, S. Li, Z. Li, H. Zhang, F. Wu, M. Xie, L. Li, R. Chen, Nano Energy **2018**, 53 524-535.
[36] S. Brunauer, P.H. Emmett, E. Teller, J. Am. Chem. Soc. **1938**, 60, 309-319.
[37] W. An, P. He, Z. Che, C. Xiao, E. Guo, C. Pang, X. He, J. Ren, G. Yuan, N. Du, D. Yang, D.-L. Peng, Q. Zhang, ACS Appl. Mater. Interfaces **2022**, 14. 10308-10318.
[38] X. Hu, X. Liu, K. Chen, G. Wang, H. Wang, J. Mater. Chem. A **2019**, 7, 11016-11037.
[39] L. Yao, Q. Gu, X. Yu, ACS Nano **2021**, 15, 3228-3240.
[40] H. Chen, M. Huang, X. Cao, S. Wei, Y. Zhao, Z. Lu, Y. Liu, L. Zhong, Y. Qiu, Chem. Eng. J. **2024**, 486, 150187.
[41] S. Tao, X. Zhang, Z. Gao, T.Y. Chen, H. Min, H. Yang, H.Y. Chen, X. Shen, J. Wang, H. Yang, Small **2023**, 19, e2304200.
[42] D. Wang, H. He, L. Han, R. Lin, J. Wang, Z. Wu, H. Liu, H.L. Xin, Nano Energy **2016**, 20, 212-220.
[43] J. Gong, R. Zhang, X. Wei, Y. Liu, Q. Luo, Q. Wan, Q. Zheng, L. Wang, S. Liu, D. Lin, Chem. Eng. J. **2023**, 459, 141609.
[44] S.H. Yang, Y.J. Lee, H. Kang, S.-K. Park, Y.C. Kang, Nano-Micro Lett. **2021**, 14, 17.
[45] Y. Ding, L. Zhang, X. Gao, M. Wei, Q. Liu, Y. Li, Z. Li, L. Cheng, M. Wu, Small **2024**, 20, 2307095.
[46] P. Li, T. Huang, Y. Lou, H. He, X. Tang, Y. Cai, M. Zhang, J. Energy Storage **2024**, 78, 109951.
[47] Y. Xu, Y. Li, T. Wang, Q. Liu, X. Fang, X. Ding, Z. Chen, C. Zhang, H. Niu, H. Zhou, H. Li, Chem. Eng. J. **2024**, 479, 147848.
[48] Z. Tang, S. Zhou, Y. Huang, H. Wang, R. Zhang, Q. Wang, D. Sun, Y. Tang, H. Wang, Electrochem. Energy Rev. **2023**, 6, 8.
[49] H. He, D. Huang, Q. Gan, J. Hao, S. Liu, Z. Wu, W.K. Pang, B. Johannessen, Y. Tang, J.L. Luo, H.

Wang, Z. Guo, ACS Nano **2019**, 13, 11843-11852.
[50] J.Y. Park, S.J. Kim, J.H. Chang, H.K. Seo, J.Y. Lee, J.M. Yuk, Nat. Commun. **2018**, 9, 922.
[51] N. Hussain, M. Li, B. Tian, H. Wang, Adv. Mater. **2021**, 33, 2102164.
[52] Q. Xiao, Q. Song, K. Zheng, L. Zheng, Y. Zhu, Z. Chen, Nano Energy **2022**, 98, 107326.
[53] D. Sha, Y. You, R. Hu, X. Cao, Y. Wei, H. Zhang, L. Pan, Z. Sun, Adv. Mater. **2023**, 35, e2211311.
[54] G. Ma, C. Li, F. Liu, M.K. Majeed, Z. Feng, Y. Cui, J. Yang, Y. Qian, Mater. Today Energy **2018**, 10, 241-248.
[55] D. Sha, Y. You, R. Hu, X. Cao, Y. Wei, H. Zhang, L. Pan, Z. Sun, Energy Storage Mater. **2023**, 58, 165-175.
[56] S. Nanda, A. Bhargav, Z. Jiang, X. Zhao, Y. Liu, A. Manthiram, Energy Environ. Sci. **2021**, 14, 5423-5432.
[57] D. Sha, Y. You, R. Hu, J. Ding, X. Cao, Y. Zhang, L. Pan, Z. Sun, Carbon Energy **2024**, e563.
[58] D. Chen, Y. Wu, Z. Huang, K. Wang, X. Zhu, Z. Wang, J. Chen, Chem. Eng. J. **2023**, 457, 141181.
[59] S. Kane, A. Storer, W. Xu, C. Ryan, N.P. Stadie, ACS Sustainable Chem. Eng. **2022**, 10, 12226-12233.
[60] K. Lei, C. Wang, L. Liu, Y. Luo, C. Mu, F. Li, J. Chen, Angew. Chem. Int. Ed. **2018**, 57, 4687-4691.